47th AIAA Aerospace Sciences Meeting Including The New Horizons Forum and Aerospace Exposition
5 - 8 January 2009, Orlando, Florida

Turbulence Modeling for Isothermal and Cryogenic Cavitation

Chien-Chou Tseng[a] and Wei Shyy[b]

[a]*Department of Mechanical Engineering and* [b]*Department of Aerospace Engineering*

University of Michigan, Ann Arbor, MI 48109

Cavitation typically occurs when the fluid pressure is lower than the vapor pressure at a local thermodynamic state. The goal of our overall efforts is to establish a predictive tool for turbulent cavitating flows, including those under cryogenic conditions with noticeable thermal effect associated with the phase change. The modeling framework consists of a transport-based cavitation model with ensemble-averaged fluid dynamics equations and turbulence closures. To date, the reported experimental investigations contain little information about the turbulent characteristics in the flow field. However, we have observed that inlet turbulent quantities can substantially impact the outcomes for cavitating flow. Because the exchange between static and dynamic pressures has a dominant impact on the cavitation dynamics, and the viscous effect can modify the effective shape of a solid object to cause noticeable variations in the predicted multiphase flow structures. A filter-based approach is utilized along with two-equation turbulence closures so that one can assess the local numerical resolution with the computed turbulence length scale, and reduce the impact of the inlet boundary conditions of the eddy viscosity. The effectiveness of the simulation framework is confirmed by using experimental data covering both isothermal and cryogenic cavitation with different geometries.

Nomenclature

σ_∞	= Cavitation number based on the free stream temperature
σ	= Cavitation number based on the local temperature
$C_{\varepsilon 1}, C_{\varepsilon 2}, \sigma_\varepsilon, \sigma_k$	= Coefficients of k-ε turbulence model
Cp	= Heat capacity
D	= Characteristic length scale
f_v	= Vapor mass fraction
h	= Enthalpy
I	= Turbulence intensity
K	= Turbulent kinetic energy
L	= Latent heat
m^+, m^-	= Source and sink terms in the cavitation model
Pr	= Prandtl number
Pt	= Production term of turbulent kinetic energy
P_v	= Saturation vapor pressure
Re	= Reynolds number
Ste	= Stefan number
T	= Temperature
t_∞	= Reference time scale, $t_\infty = L/U_\infty$
U_∞	= Reference velocity
u	= Velocity

Δv = Difference of specific volume during phase change in Clapeyron equation

x = Space variable

α_l = Liquid volume fraction

ρ = Density

μ = Dynamic viscosity

$\mu_T/\mu_L|_{inlet}$ = Eddy-to-laminar viscosity ratio at the inlet

$\emptyset_m$ = Mixture property

ε = Turbulent dissipation rate

Δ = Filter size in filter-based model

δ^* = Displacement thickness

Subscript

j = Component

l = Liquid

L = Laminar

m = Mixture property

T =Turbulent

v = Vapor

ω =Free stream quantities

1. Introduction

Cryogenic liquids, including oxygen, nitrogen, and hydrogen, are popular fuels for the commercial launch vehicle as propellants because the by-products are clean and the power/gallon ratio is high. A key design issue related to rocket fuel and oxidizer pumps is the minimum pressure that the design can tolerate for a given inlet temperature and rotating speed. To keep inlet pressure low (reduce tank weight) and pump rotational speeds high (reduce engine weight), cavitation is prone to appear in the inducer section. To date, there is no established method capable of predicting the actual loads due to cavitation on the inducer blades. The unsteadiness of the cavitating pump can couple with the feed or discharge system to cause large component oscillations. Virtually every rocket engine system designed in the U.S. has experienced issues with cavitating elements in the pump. This includes recent programs like ATP turbopumps for the SSME, the Fastrac LOX pump, and the RS-68 commercial engine. An integrated framework based on computational modeling and control strategies is desirable to treat this critical and difficult issue.

Cavitation typically occurs when the fluid pressure is lower than the vapor pressure at a local thermodynamic state [1,2,3,4]. For fluids such as water, due to a very large ratio between liquid and vapor densities, around $O(10^5)$, thermal effects are insignificant during cavitation process. For cryogenic fluids, the liquid/vapor density ratios are not as high, and other quantities such as latent heat and thermal conductivity can influence the thermal field more substantially than for water. Representative values of these quantities and the pressure-temperature saturation curves are listed and illustrated in table 1 and Figure 1, respectively: the cryogenic fluids such as nitrogen have significantly higher slopes of pressure-temperature saturation curve than water [5], indicating that the vapor pressure can vary substantially due to the thermal effect. Based on the Clapeyron equation [6] at representative working temperatures:

$$\frac{dP_v}{dT} = \frac{L}{T\Delta v} \tag{1}$$

The sensitivity of the vapor pressure with respect to temperature for liquid nitrogen and hydrogen are 20kPa/K and 28kPa/K, respectively, and only 0.19kPa/K for water. Consequently, the local temperature drop due to the evaporative cooling is non-negligible in cryogenic liquids, and the energy transport needs to be included in the cavitation model [7,8]. Moreover, with 1˚C as temperature difference ΔT for liquid nitrogen and hydrogen, the Stefan number $Ste=Cp\Delta T/L=$ 0.01 and 0.02 respectively; hence the sensible heat is much smaller than the latent heat. Under this *Ste*, the cavity growth rate or interfacial velocity will be vey small.

The dynamic similarity for isothermal case, such as water is governed by the cavitation number $\sigma_\infty = \dfrac{P_\infty - P_v}{0.5\rho_l U_\infty^2}$ [1,2,8] based on a constant vapor pressure $Pv(T_\infty)$. For cryogenic cavitation, the actual local cavitation number σ needs to be corrected according to the local temperature: $\sigma = \dfrac{P_\infty - P_v(T)}{0.5\rho_l U_\infty^2}$. By the following first order approximation [8]:

$$\frac{1}{2}\rho_l U_\infty^2(\sigma - \sigma_\infty) = \frac{dp_v}{dT}(T_\infty - T) \qquad (1)$$

Equation (2) clearly shows the temperature dependency of cavitation, and the local temperature drop in cryogenic cavitation will produce a noticeable rise for the local cavitation number σ and hence suppress the cavitation intensity [7]. The detail impact for the thermal-sensible material properties to cavitation model will be introduced later.

The numerical modeling of cavitation largely follow two main categories: interface tracking methods with individual phases separately treated [9,10], and homogeneous flow models based on a single-fluid framework with fluid properties estimated based on the liquid-vapor mixture ratios [7,8,11,12,13,14,15,16,17,19,20,21]. Differences between the various models in the second category mostly come from the relation that defines the density field. For overview of the various modeling approaches, see, e.g., [7,8,11,17].

A popular homogeneous flow model utilizes the framework of the transport-based equation (TEM) [7,8,11,12,17], which is adopted in the present study. In this method, the information of the vapor volume/mass fraction distribution is obtained in a modeled transport equation based on the mass transfer between vapor and liquid phases. This approach is well documented, see, e.g., [7,8,11,17].

For turbulence, the ensemble-averaged modeling with a two-equation closure [22] along with a filter-based model (FBM) [17,18] is utilized. The approach reduces the influence of the turbulent eddy viscosity based on the local numerical resolution, essentially blending direct numerical simulation (DNS) and conventional turbulence model in a single framework. Specifically, the level of the turbulent viscosity is corrected by comparing the turbulence length scale computed from the turbulence closure and the filter size Δ based on the local mesh spacing. As will be discussed in detail, the uncertainty associated with inlet turbulent quantities can substantially impact the outcome of the conventional two-equation eddy viscosity model. The filter-based approach can effectively improve the consistency of the numerical predictions by reducing the reliance on the turbulence closure.

To date, the sensitivity of the turbulent cavitating flow simulations with respect to inlet turbulent quantities has not been adequately examined for cavitating flow. The present study is aimed at addressing some of these issues for both isothermal and cryogenic cavitation.

2. Governing Equations and Numerical Techniques

The set of governing equations for cryogenic cavitation under the homogeneous-fluid modeling consists of the conservative form of the Favre-averaged Navier-Stokes equations, the enthalpy-based energy equation (for cryogenic cavitation), the k-ε two-equation turbulence closure, and a transport equation for the liquid volume fraction [7,8,11,17]. The continuity, momentum, enthalpy, and cavitation model equations are given below. All computations presented below are based on the steady-state equations.

$$\frac{\partial(\rho_m u_j)}{\partial x_j} = 0 \tag{2}$$

$$\frac{\partial(\rho_m u_i u_j)}{\partial x_j} = -\frac{\partial p}{\partial x_i} + \frac{\partial}{\partial x_j}[(\mu_L + \mu_T)(\frac{\partial u_i}{\partial x_j} + \frac{\partial u_j}{\partial x_i} - \frac{2}{3}\frac{\partial u_k}{\partial x_k}\delta_{ij})] \tag{3}$$

$$\frac{\partial}{\partial x_j}[\rho_m u_j (h + f_v L)] = \frac{\partial}{\partial x_j}[(\frac{\mu_m}{\mathrm{Pr}_m} + \frac{\mu_T}{\mathrm{Pr}_T})\frac{\partial h}{\partial x_j}] \tag{4}$$

$$\frac{\partial(\alpha_l u_j)}{\partial x_j} = \dot{m}^+ + \dot{m}^- \tag{5}$$

The mixture property, $\emptyset_m$, enthalpy, and the vapor mass fraction are respectively expressed as:

$$\phi_m = \phi_l \alpha_l + \phi_v (1 - \alpha_l) \tag{6}$$

$$h = C_{Pm} T \tag{7}$$

$$f_v = \frac{\rho_v (1 - \alpha_l)}{\rho_m} \tag{8}$$

We neglect the effects of kinetic energy and viscous dissipation terms in Equation (4) ($O(Re^{-0.5})$, Re is around 10^6) because the temperature field is mainly contributed by the evaporative cooling in cryogenic cavitation.

(i). Transport-Based Cavitation Model

The source term $\dot{m}^+$ and sink term $\dot{m}^-$ in Equation (6) represent for condensation and evaporation rates. They have been derived from various aspects, including dimensional argument with empirical support [7,8,11,12,13,14,15,16,17], force balance based on the interfacial dynamics [8,11,12], and estimate of the bubble growth rate through the Rayliegh-Plesset equation [19,20,21]. Numerically, [7,8,11,12,14,15,17] utilized pressure-based methods, and [13,16,19,20,21] employed the density-based methods. The liquid-vapor evaporation and condensation rates for the present transport-based cavitation model [7,8,11,12,13,17] are respectively shown as following:

$$\dot{m}^- = \frac{C_{dest}\rho_l \mathrm{Min}(0, p - p_v)\alpha_l}{\rho_v (0.5\rho_l U_\infty^2) t_\infty} \qquad \dot{m}^+ = \frac{C_{prod}\mathrm{Max}(0, p - p_v)(1 - \alpha_l)}{(0.5\rho_l U_\infty^2) t_\infty} \tag{9}$$

where C_{dest} and C_{prod} are the empirical constants, U_∞ is the reference velocity scale, and t_∞ is the reference time scale, which is the characteristic length scale L divided by the reference velocity scale U_∞ ($t_\infty = L/U_\infty$). For non-cryogenic fluids like water, the constants are specified C_{dest} =1 and C_{prod} =80 [11,13]. As for liquid nitrogen, from numerical experimentation, the constants are chosen as C_{dest} =0.639 and C_{prod} =54.4, and for liquid hydrogen, C_{dest} =0.767 and C_{prod} =54.4 are suggested [7].

For cryogenic cavitation simulations, the temperature dependent properties are updated from a comprehensive data base [5] throughout the course of computations in every iteration.

(ii). Thermodynamics Effects

The impact of thermal effects in cryogenic cavitation due to phase change on temperature prediction has been already shown in Figure 1. These thermo-sensible material properties will affect the energy equation in Equation (5) and cavitation sink/source terms in Equation (10).

First, the latent heat L in Equation (5) appears as a non-linear source term and represents the latent heat transfer

rate during the phase change. The spatial variation of the thermodynamic properties together with the evaporative cooling effect is embedded into this equation and causes a coupling with the set of governing equations [7].

As for the cavitation sink/source terms in Equation (10), we can assess the impacts due to the thermo-sensible material properties by using Taylor's series and neglect the higher order terms. We first consider the sink term $\dot{m}^-$ as the pressure is smaller than the vapor pressure [7]:

$$\begin{aligned}\dot{m}^- &= \frac{C_{dest}\alpha_l}{t_\infty}\frac{\rho_l}{\rho_v}\frac{p-p_v(T)}{0.5\rho_l U_\infty^2} = \beta R(T)\sigma(T) \\ &= \beta(R(T_\infty)+\left.\frac{dR}{dT}\right|_{T_\infty}\Delta T+...)(\sigma(T_\infty)+\left.\frac{dp_v}{dT}\right|_{T_\infty}\frac{\Delta T}{0.5\rho_l U_\infty^2}+...) \\ &= \beta(R(T_\infty)\sigma(T_\infty)+\sigma(T_\infty)\left.\frac{dR}{dT}\right|_{T_\infty}\Delta T+R(T_\infty)\left.\frac{dp_v}{dT}\right|_{T_\infty}\frac{\Delta T}{0.5\rho_l U_\infty^2}+...)\end{aligned} \tag{10}$$

Where β is $\boldsymbol{C_{dest}\alpha_l/t_\infty}$ and R is the temperature-dependent liquid/vapor density ratio, and σ is the cavitation number based on the local vapor pressure. Similarly for source term $\dot{m}^+$ as the pressure is larger than the vapor pressure:

$$\begin{aligned}\dot{m}^+ &= \frac{C_{prod}(1-\alpha_l)}{t_\infty}\frac{p-p_v(T)}{0.5\rho_l U_\infty^2} = \gamma\sigma(T) \\ &= \gamma(\sigma(T_\infty)+\left.\frac{dp_v}{dT}\right|_{T_\infty}\frac{\Delta T}{0.5\rho_l U_\infty^2}+...)\end{aligned} \tag{11}$$

Where γ is $\boldsymbol{C_{prod}(1-\alpha_l)/t_\infty}$.

It can be concluded that the competing influence of the thermal effects in the cavitation model comes from two ways: (1) thermal rate of change of liquid/vapor density ratio $\boldsymbol{dR/dT|_{T_\infty}}$ which is negative in Figure 1 (c) and (2) thermal rate of change of vapor pressure $\boldsymbol{dP_v/dT|_{T_\infty}}$ which is positive in Figure 1 (a).

It is obvious that the impacts of thermal effects will change significantly for different working temperature and pressure due to the non-linear variation of material properties from energy equation in Equation (5) and cavitation sink/source terms in Equation (10).

(iii). Turbulence Model

The k-ε two-equation turbulence model with a wall function treatment is presented as follows [22,10]:

$$\frac{\partial(\rho_m u_j k)}{\partial x_j} = \mathrm{P}_t - \rho_m\varepsilon + \frac{\partial}{\partial x_j}[(\mu_L+\frac{\mu_T}{\sigma_k})\frac{\partial k}{\partial x_j}] \tag{13}$$

$$\frac{\partial(\rho_m u_j \varepsilon)}{\partial x_j} = C_{\varepsilon_1}\frac{\varepsilon}{k}\mathrm{P}_t - C_{\varepsilon_2}\rho_m\frac{\varepsilon^2}{k} + \frac{\partial}{\partial x_j}[(\mu_L+\frac{\mu_T}{\sigma_\varepsilon})\frac{\partial\varepsilon}{\partial x_j}] \tag{14}$$

where the production term of turbulent kinetic energy (P_t) and the Reynolds stress tensor are defined as:

$$\mathrm{P}_t = \tau_{ij}\frac{\partial u_i}{\partial x_j};\ \tau_{ij} = -\overline{\rho_m u_i' u_j'}$$
$$\overline{\rho_m u_i' u_j'} = \frac{2\rho_m k\delta_{ij}}{3} - \mu_T\left(\frac{\partial u_i}{\partial x_j} + \frac{\partial u_j}{\partial x_i}\right) \quad (15)$$

with $C_{\varepsilon 1} = 1.44$, $C_{\varepsilon 2} = 1.92$, $\sigma_\varepsilon = 1.3$, $\sigma_k = 1.0$. The turbulent eddy viscosity is defined as:

$$\mu_T = \frac{\rho_m C_\mu k^2}{\varepsilon},\ C_\mu = 0.09 \quad (16)$$

As mentioned above, a filter-based model (FBM) [17,18] is also adopted. This model limits the influence of the eddy viscosity based on the local numerical resolution, essentially forming a combined direct numerical simulation and RANS model. Specifically, the level of the turbulent viscosity is corrected by comparing the turbulence length scale and the filter size Δ, which is based on the local meshing spacing:

$$\mu_T = 0.09\rho_m \frac{k^2}{\varepsilon} MIN\left(1,\ \frac{\Delta\cdot\varepsilon}{k^{3/2}}\right) \quad (17)$$

By imposing the filter, the turbulence length scale will not be resolved if it is smaller than the filter size. The filter size is chosen to be comparable to the maximum grid size.

$$\Delta = MAX(\Delta_{present}, \Delta_{grid}) \quad (18)$$

Thus if the grid resolution is significantly smaller than the turbulence length scale in the entire flow field, the solution will approach that of a direct numerical simulation; for inadequately resolved computations, the RANS model is recovered.

(iv). Numerical method

Detailed numerical procedures for the cavitation model and associated fluid dynamics equations adopted here utilize a modified pressure-based approach for large density jump as well as thermal effects, as reported in [7,8,11] The controlled variation scheme (CVS) [11,12,22] is applied to discretize the convection scheme, and central difference is used for both pressure and diffusion terms. The CVS scheme can prevent the oscillations under sharp gradients caused by the phase change while preserving second-order accuracy elsewhere.

As for the boundary conditions, liquid volume fraction, velocity, temperature and turbulent quantities are specified at the inlet. For the outlet, pressure and other flow variables are extrapolated. On the walls, pressure, liquid volume fraction, and turbulent quantities are extrapolated along with no-slip and adiabatic conditions. Additionally, the pressure at the reference point (P_∞) in the upstream is also fixed to define the cavitation number σ_∞ [11,12].

Based on the eddy-tolaminar viscosity ratio at the inlet, $\mu_T / \mu_L|_{inlet}$, the inlet turbulent quantities can be given as following:

$$k = \frac{3}{2}(U_\infty I)^2,\quad \varepsilon = \frac{k^2}{\nu_L(\mu_T / \mu_L|_{inlet})} \quad (19)$$

where I is turbulence intensity, which is 0.02 here. Without experiental guidance, the inlet considtions are selected to allow the eddy-to-laminar viscosity ratio at the inlet, $\mu_T / \mu_L|_{inlet}$, to vary. This is a main focus of this study, as will be presented next.

3. Results and Discussion

There are several geometries simulated here: for water, a hemispherical projectile with the experimental measurements by Rouse and McNown [24] (Figure 2(a)) and the NACA66MOD hydrofoil with the experimental measurements by Shen and Dimotakis [25] (Figure 2(b)) are investigated; for cryogenic nitrogen, a 2D quarter hydrofoil with the experimental measurements by Hord [26] (Figure 2(c)) are considered. Figure 2 also shows the corresponding boundary conditions for each geometry.

(i) ***Isothermal cavitation***

First, we present results based on isothermal modeling for water around a hemispheric projectile (Figure 2(a), number of grid points=7.8×10^3) and the NACA66MOD hydrofoil (Figure 2 (b), number of grid points=3.3×10^4).

For the hemispherical projectile, an axisymmetric case, the Reynolds number is 1.36×10^5, and the cavitation number σ_∞ is 0.4. There is no information regarding the inlet turbulent variables, and three different inlet turbulent quantities are presented here. With turbulence intensity=0.02, the dissipation rate is adjusted, resulting in the inlet eddy-to-laminar viscosity ratio of 1.5×10^2, 5×10^2, and 10^3, and the effective Reynolds number (based on the eddy viscosity) of 900, 270, and 136, respectively. For the NACA66MODE hydrofoil (angle of attack of 4°), the Reynolds number and the cavitation number σ_∞ are 2×10^6 and 0.91, respectively. In this case, we assign the inlet eddy-to-laminar viscosity ratio of 10^3, 2×10^3, and 10^4, corresponding to the effective Reynolds number of 2000, 1000, and 200. With the baseline k-ε model (no filter), the cavity shapes and the liquid volume fraction distributions are highlighted in Figure 3 based on the viscosity ratio 1.5×10^2 (effective *Re*=900) for the hemispherical projectile and 10^3 (effective *Re*=2000) for the NACA66MODE hydrofoil. The wall pressure distribution along with the experimental data [24,25] and liquid volume fraction α_l corresponding to different inlet turbulent quantities are shown in Figure 4.

The results in Figure 4 show much higher dependency of inlet turbulent quantities for NACA66MOD hydrofoil than for the hemispherical projectile. Efforts have been made to elucidate the mechanisms responsible for these diverging trends. First, Figure 5 simply confirms that for high Reynolds number flows, overall, the dynamic pressure is much larger than the shear stress. In general, cavitation appears largely from the exchange between dynamic and static pressure locally. However, the viscous effect can significantly modify the effective shape of a solid object by using the concept of displacement thickness defined along the direction normal to a solid surface:

$$\delta^* = \int_0^\infty (1 - \frac{\rho u}{(\rho u)_\infty}) dn \tag{20}$$

For the hemispherical projectile, Figure 6(a) shows that profiles of the displacement thickness for different inlet turbulent quantities are consistent except near s/D=0. However, since cavitation occurs in the straight section of the projectile, the effective object shape modified by δ^* doesn't affect the sink term m^- and the source term m^+ in the cavitation model as illustrated in Fig. 6(b) so that the cavity size and mixture density inside the cavity in Figure 4(a) and (c) are comparable for different inlet turbulent quantities.

For the NACA66MOD hydrofoil, as shown in Figure 7(a), the displacement thickness varies between the different inlet conditions, and consequently affects the pressure field and cavitation formation. Due to a smaller mixture density after the leading edge for a lower inlet eddy-to-laminar viscosity ratio in Figure 4(d), the displacement thickness becomes larger in Figure 7(b) and hence give a stronger sink (evaporation) term m^- in Figure 7(c). As for the source (condensation) term m^+, a lower inlet eddy-to-laminar viscosity ratio gives a smaller value, and combining with a larger sink term results in a larger cavity size. As the results, the cavity size is more sensitive for different inlet turbulent quantities, and the cavity size is larger as inlet eddy-to-laminar viscosity ratio becomes smaller in this case.

Using FBM with a filter size Δ=1.5 times the maximum grid size to NACA66MOD hydrofoil, the displacement thicknesses of all cases considered in Figure 8(a) become insensitive to the inlet turbulent quantities, and hence pressure distributions, shown in Figure 8(b), and other variables are also comparable for different inlet conditions.

Figure 9, Figure 10, and Figure 11 explain how the filter helps reduce the sensitivity of the solution with respect to the inlet conditions. For a higher inlet eddy-to-laminar viscosity ratio, the filter function $MIN(1\ ,\ \Delta/(k^{3/2}/\varepsilon))$ is lower, and the numerical resolution of the grid adopted here is sufficient to produce solutions with less dependence of the turbulence model. Hence, the eddy viscosity is lowered after the inlet region, resulting in reduced sensitivity of the computations. Based on this observation, even though FBM is not invoked in the near wall region due to the wall function treatment, it still can affect the overall solutions. Figure 12 clearly shows the eddy viscosity in the near wall region is reduced after using FBM.

(ii) Cryogenic cavitation

Cavitation with thermal effect for the cryogenic liquids past a 2D quarter hydrofoil, illustrated in Figure 2(c) with number of grids=2×10^4, will be presented here. The Case 290C and 296B from the experimental data reported by Hord [26] are investigated with the following conditions: σ_∞=1.7, Re=9.1×10^6, T_∞=83.06K for 290C; σ_∞=1.61, Re=1.1×10^7, T_∞=88.54K for 296B both with liquid nitrogen. In the following, based on Case 290C and 296B, we present assessment of the thermal effect on cavitating flow structures.

Figure 13 and Figure 14 compare the predicted and experimentally measured pressure and temperature profiles [26] on the hydrofoil surface. Overall, the present cavitation and turbulence models with filter (FBM) can consistently capture the main features of both pressure and thermal profiles. The temperature drop inside the cavity in Figure 13(b) and Figure 14(b) also clearly demonstrates the evaporative cooling resulting from cryogenic cavitation. In Figure 15, as a further assessment based on Case 290C, we compare the present cryogenic model solution with the isothermal solution, obtained by using the identical model except that the energy equation is not invoked. Clearly, the thermal field does affect the cavity structures. The cavity size is reduced due to the thermal effect because the temperature drop inside the cavity decreases the local vapor pressure and hence increases the local cavitation number, resulting in a weaker cavitation intensity. Furthermore, the thermal effect makes the cavitation sink term m^- and source term m^+ in Equation (11) and (12) become weaker and stronger, respectively, resulting in higher overall liquid volume fraction in the cavity (as shown in Figure 15(c)). Finally, in Figure 15(d), the pressure profile inside the cavity is steeper under the cryogenic condition than that under the isothermal condition.

We show the thermal effects by comparing the local cavitation number $\sigma=\dfrac{P_\infty-P_v(T)}{0.5\rho_l U_\infty^2}$ contours and temperature contours in Figure 16 and Figure 17. The free stream cavitation number of Case 296B (σ_∞=1.61, T_∞=88.54K) is smaller than that of Case 290C (σ_∞=1.7, T_∞=83.06K). However, the evaporative cooling and associated factors such as the gradient of the vapor pressure increase as temperature approaches critical temperature as shown in Figure 1(a). This effect causes a greater increase in local cavitation number σ inside the cavity for Case 296B in Figure 17. Therefore the thermal field affects the effective cavitation number as well as the cavity width and height.

4. Summary and Conclusions

A computational modeling framework has been further developed for both isothermal and cryogenic cavitation. The model consists of a transport-based cavitation model with refined modeling parameters [7,8], a filter-enhanced turbulence closure, and an algorithm capable of handling large property jumps as well as non-isothermal conditions [7,8,11]. Several geometries are selected for water as well as cryogenic fluids. A main focus of this work is to address the uncertainty associated with the inlet turbulent quantities.

For high Reynolds number flows, while cavitation appears largely from the exchange between dynamic and static pressure locally, the viscous effect can significantly modify the effective shape of a solid object, the pressure distributions, and the cavitation dynamics. For the hemispheric projectile with the cavitation number investigated

here, the cavitation occurs in the straight cylindrical portion of the projectile, and the effect of the displacement thickness on the cavitation process is minor. For the NACA66MOD hydrofoil, the pressure distribution is noticeably more sensitive to the displacement thickness because it modifies the local curvature of the airfoil in noticeable manners. It is shown that the filter-based model can help reduce the impact of the uncertainty assciated with the conventional two-equation model and the inlet turbulent quantities by reducing the reliance of eddy viscosity.

For cryogenic cavitation, the evaporative cooling reduces cavitation intensity and results in a shorter cavity size than that under isothermal conditions. The thermal field shows noticeable impact on the effective cavitation number as well as the cavity width and height.

5.Acknowledgements

The present efforts have been supported by the NASA Constellation University Institutes Program (CUIP), Claudia Meyer and Jeff Rybak project managers.

6.References

[1] Knapp R.T. , Daily J.W. and Hammitt F.G., "Cavitation. McGraw-Hill", New York, 1970.

[2] Brennen C.E., "Cavitation and Bubble Dynamics", Oxford Engineering & Sciences Series 44, Oxford University Press. 1995.

[3] Joseph D.D., "Cavitation in a Flowing Liquid", Phys. Review E, 1995, vol 51, issue 3, 1649-1650,.

[4] Joseph D.D.,"Cavitation and the State of Stress in a Flowing Liquid", Fourth International Symposium on Cavitation. 2001.

[5] Lemmon E.W., McLinden M.O., and Huber M.L.,. "REFPROP: Reference Fluid Thermodynamic and Transport Properties", NIST Standard Database 23, version 7.0, 2002.

[6] Sonntag R. E., Borgnakke C, and Wylen G .J., " Fundamentals of thermodynamics", John Wiley and Sons, Inc. 2004.

[7] Goel T., Zhao J., Thakur S., Haftka R. T., Shyy W., and Zhao J., "Surrogate Model-Based Strategy for Cryogenic Cavitation Model Validation and Sensitivity Evaluation", Int. J. Numer. Meth. Fluids, 2008,vol 58, pp. 969-1007.

[8] Utturkar Y., Wu J., Wang G., and Shyy W., "Recent Progress in Modeling of Cryogenic Cavitation for Liquid Rocket Propulsion. Progress in Aerospace Sciences", OCT,2005,vol. 41, no. 7, pp. 558-608, .

[9] Chen Y., and Hesiter S. D., "A Numerical Treatment for Attached Cavitaition"; J Fluids,1994, vol. 116, pp 613-618.

[10] Deshpande M., Feng J., and Merkle C.L., "Numerical Modeling of the Thermodynamic Effects of Cavitation",J. Fluids Eng, 1997,vol 119, pp420-427.

[11] Senocak I., and Shyy W., "Interfacial Dynamics-Based Modeling of Turbulent Cavitating Flows", Part-1: Model Development and Steady-State Computations", International Journal for Numerical Methods in Fluids, 2004,vol.44, pp975-995.

[12] Senocak I., and Shyy W., "Interfacial Dynamics-Based Modeling of Turbulent Cavitating Flows", Part-2: Time-Dependent Computations", International Journal for Numerical Methods in Fluids, 2004, vol. 44, pp997-1016/

[13] Merkle, C.L., Feng J., and Buelow, "PEO. Computational Modeling of Sheet Cavitation", Proc. 3rd International Symposium on Cavitation, Grenoble, France, 1998.

[14] Singhal A.k., Vaidya N., and Leonard A.D.," Multi-Dimensional Simulation of Cavitating Flows Using a PDF Model for Phase Change.ASME Paper",FEDSM 97-3272, The ASME Fluids Engineering Division Summer Meeting, 1997.

[15] Singhal A.k., Li H, Athavale, M.M., and Jiang Y., "Mathematical Basis and Validation of the Full Cavitation Model", ASME Paper FEDSM2001-18015, The ASME Fluids Engineering Division Summer Meeting, 2001.

[16] Kunz R.F., Boger D.A., stinebring D.R., Chyczewski T.S., Lindau, J.W., Gibeling H.J., Venkateswaran S, Govindan., "TR. A preconditioned Navier –stokes method for two phase flows with application to cavitation prediction, comput Fluids",2000, vol. 29, pp 849-875.

[17] Wu J.Y., "Filter Based Modeling of Unsteady Turbulent Cavitating Flow Computational. Dissertation of Doctor of Philosophy in University of Florida", 2005.

[18] Wu J.Y., and Shyy W., "Filter Based Unsteady RANS Computational. International Journal of Heat and Fluid Flow", 2004, vol. 25, pp. 10-21.

[19] Hosangadi A., and Ahuja V., "A Numerical of Cavitation in Cryogenic Fluids Part II; New Unsteady Model for Dense Cloud Cavitation", 6th International Symposium on Cavitation, Sep. 2006, Wageningen, Netherlands.

[20] Aliabadi S., Tu S.Z., and Watts M.D., "Simulation of Hydrodynamic Cavitating Flows Using Stabilized Finite Element Method", 43th AIAA Aerospace Science Meeting and Exhibit, Jan. 2005, Reno, Nevada.

[21] Giorgi M.G.D., Ficarella A., Chiara F., and Laforgia D., "Experimental and Numerical Investigations of Cavitating Flows", 35th AIAA Fluids Dynamics Conference and Exhibit , Jun. 2005, Toronto, Ontario Canada.

[22] Launder B.E., and Spalding D.B., "The Numerical Computation of Turbulent Flow",Comp. Meth. Appl. Mech. Eng.. 1974,vol 3, pp269-289.

[23] Shyy W., Thakur S.S., Ouyang, H., Liu J.,and Blosch E., "Computational Techniques for Complex Transport Phenomenon. Cambridge University Press", 2007.

[24] Rouse H, and McNown, J.S., "Cavitation and Pressure Distribution, Head Forms at Zero Angle of Yaws Flow Phenomenon", Studies in Engineering, Bulletins 32, State University of Iowa, 1948.

[25] Shen Y., and Dimotakis, P., "The Influence of Surface Cavitation on Hydrodynamic Forces. Proc", 22nd. ATTC, St. Johns, 1989,pp. 44-53,

[26] Hord J., "Cavitation in Liquid Cryogens", II-Hydrofoil. NASA CR-2156 1973.

Substance	*Cp* (J/Kg K)	Density ratio	Thermal conductivity (W/mK)	*L (KJ/Kg)*	Δv
Water (298k)	4200	43220	681	2442	43.35
N_2 (83k)	2075	95	134	190	0.12
H_2(20k)	9484	57	103	446	0.79

Table 1. Variation of physical properties for water (298k), liquid nitrogen (83k), and liquid hydrogen (22k) on saturation curves. [5]

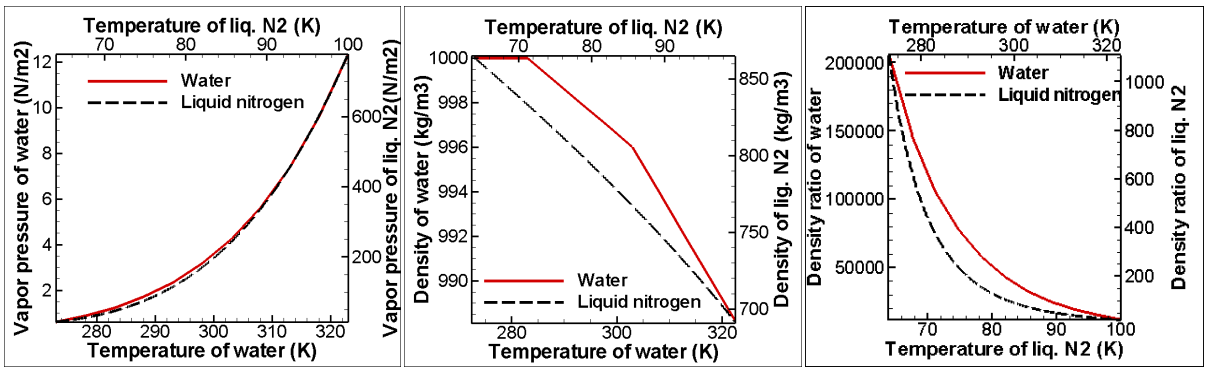

(a)Vapor pressure vs. temperature (b)Liquid density vs. temperature (c)Density ratio (liq./vapor) vs. temperature

(Solid lines represnt for water and use bottom and left as x-axis and y-axis in each figure; dash lines represnt for liquid nitrogen and use top and right as x-axis and y-axis in each figure)

Figure 1. Variation of physical properties for liquid nitrogen and water along saturation curve. [5]

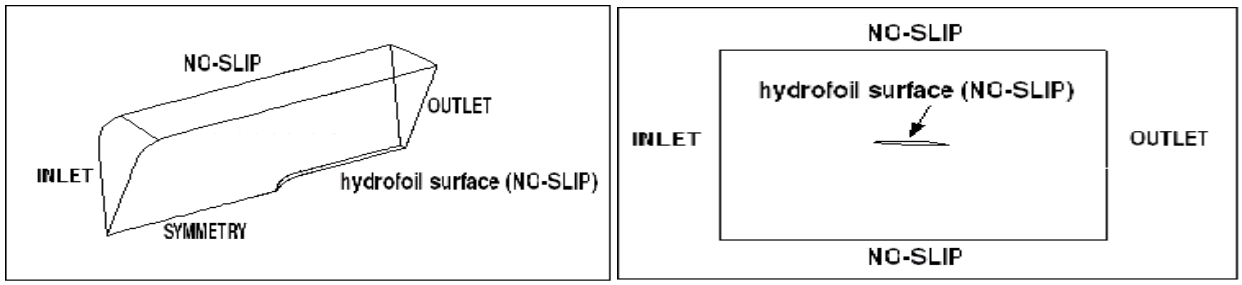

(a) Hemi. projectile for isothermal cavitation [24] (b) NACA66MOD hydrofoil for isothermal cavitation [25]

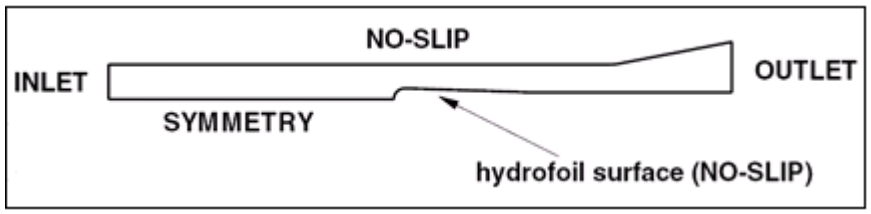

(c) 2D quarter hydrofoil for cryogenic cavitation [26]

Figure 2. Schematic of the geometries and the boundary conditions of the cases considered.

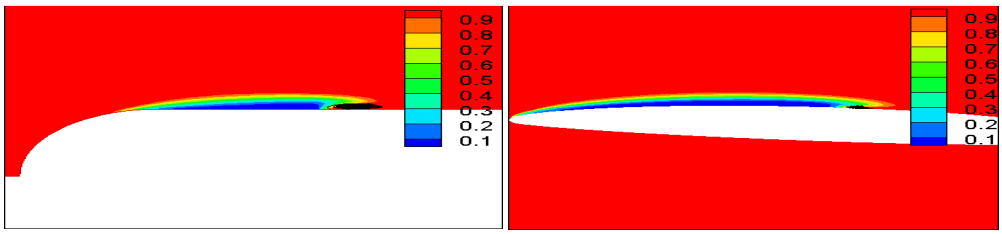

(a) Hemispherical projectile, $\mu_T/\mu_L|_{inlet}$=1.5 × 10^2 , and effective *Re*=900 (b) NACA66MODE hydrofoil, $\mu_T/\mu_L|_{inlet}$=10^3 ,and effective *Re*=2000

Figure 3. The liquid volume fraction contour and cavity shape for isothermal cases by baseline k-ε model

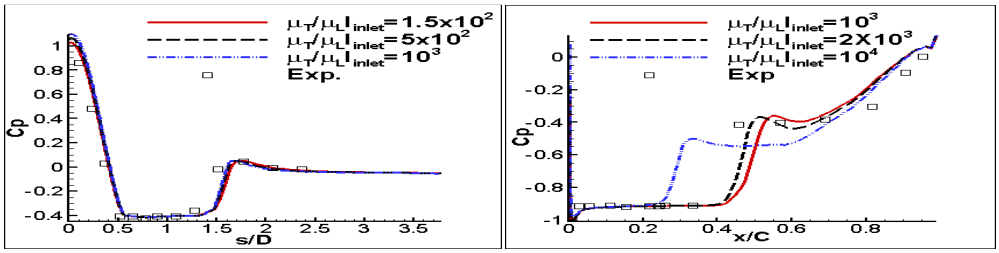

(a) *Cp* , hemispherical projectile (b) *Cp* , NACA66MODE hydrofoil

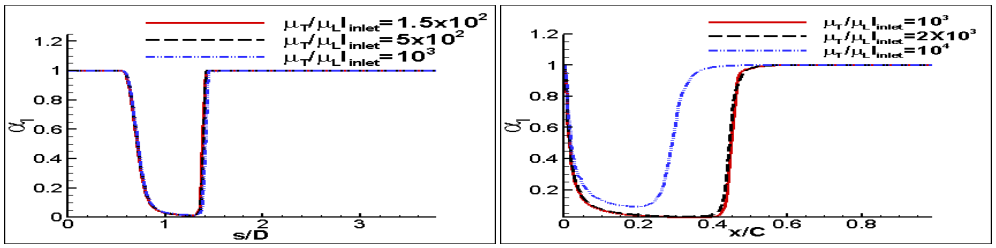

(c) α_l , hemispherical projectile (d) α_l , NACA66MODE hydrofoil

Figure 4. *Cp* and α_l along surface of different $\mu_T/\mu_L|_{inlet}$, isothermal cases by baseline k-ε model (without filter)

(For hemi. projectile, 1.5 × 10^2, 5 × 10^2, and 10^3correspond the effective *Re* of 900, 270, and 136; for NACA66MOD hydrofoil, 10^3, 2 × 10^3, and 10^4correspond the effective *Re* of 2 × 10^3,10^3, and 10^2. D is the diameter of hemispherical front, and C is the chord length of NACA66MODE hydrofoil)

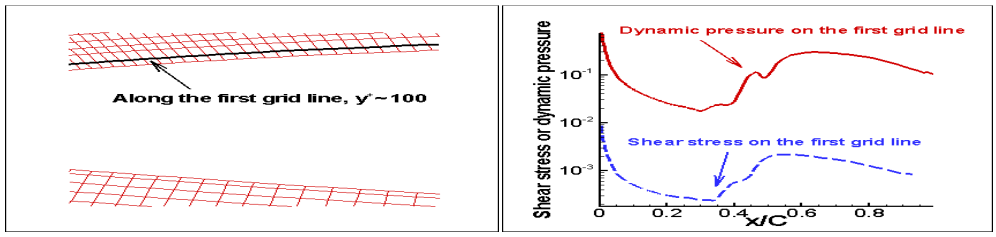

(a) Layout of first grid line (b) Dynamic pressure vs. shear stress on first grid line

Figure 5. Near-wall grid layout and quantities along the first grid line of NACA66MODE hydrofoil

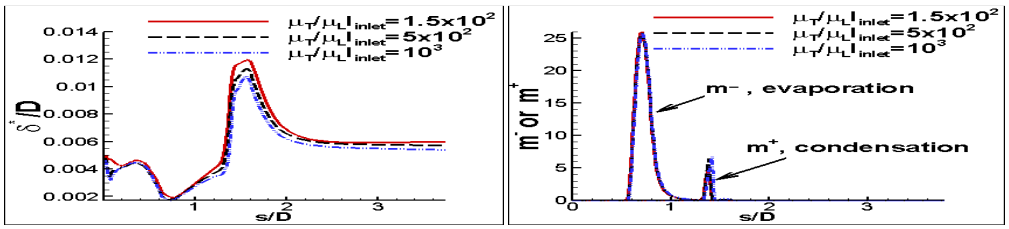

(a) δ^* (b) m^-or m^+along the first grid line

Figure 6. Associated flow variables for hemispherical projectile along surface by baseline k-ε model

(s denotes distance along the surface and D is the diameter of hemispherical front)

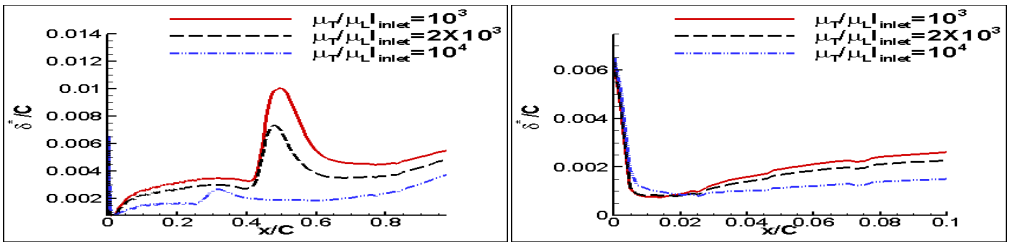

(a) δ^* (b) δ^* near trhe leading edge

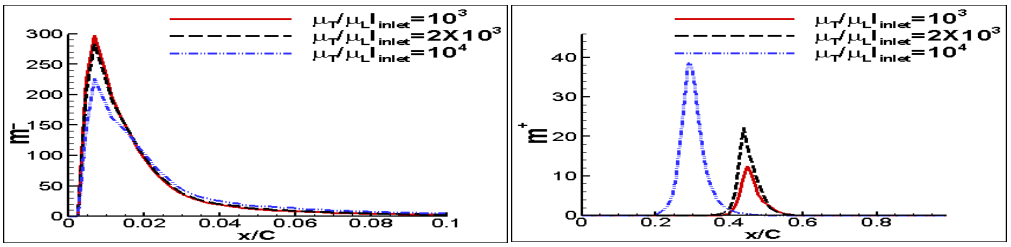

(c) m^- along the first grid line (d) m^+ along the first grid line

Figure 7. The various flow variables and cavitation model terms for the NACA66MODE hydrofoil by using the baseline k-ε model(10^3, 2×10^3, and 10^4 corresponds to effective *Re* of 2000, 1000, and 200 respectively)

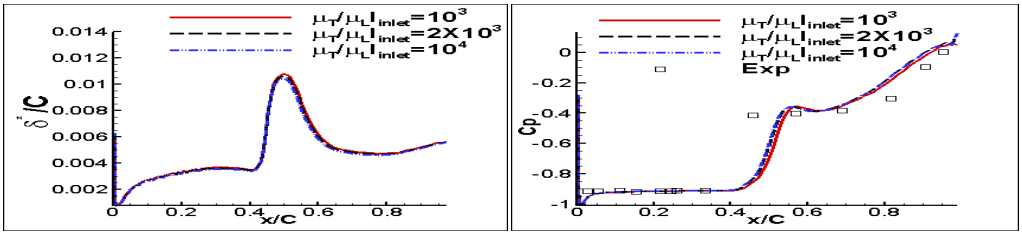

(a) δ^* (b) Cp

Figure 8. Results after using FBM with Δ=1.5 maximum grid size for NACA66MODE hydrofoil

(10^3, 2×10^3, and 10^4 corresponds to effective *Re* of 2000, 1000, and 200respectively)

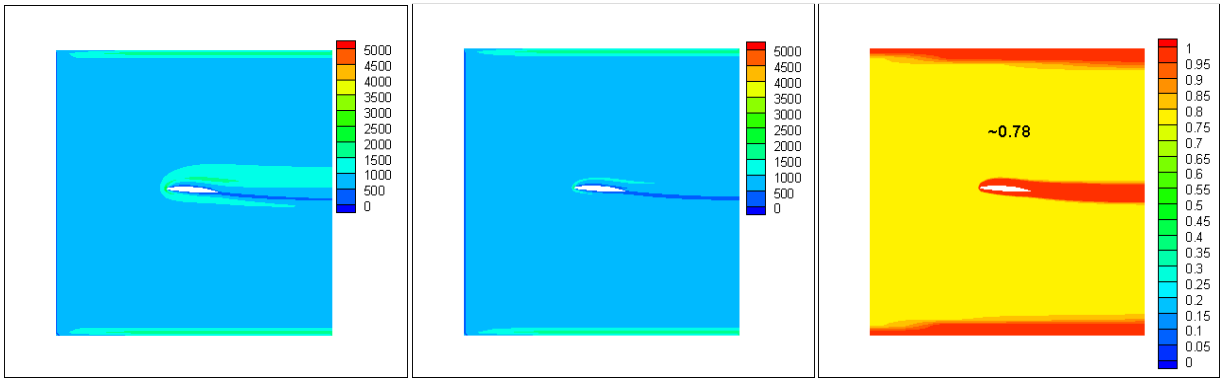

(a) μ_T/μ_L before FBM (b) μ_T/μ_L with FBM (c)$MIN(1,\Delta/(\,k^{1.5}/\varepsilon)$

Figure 9. Comparisons before/after FBM for NACA66MODE hydrofoil, $\mu_T/\mu_L|_{inlet}$=10^3,effective *Re*= 2000

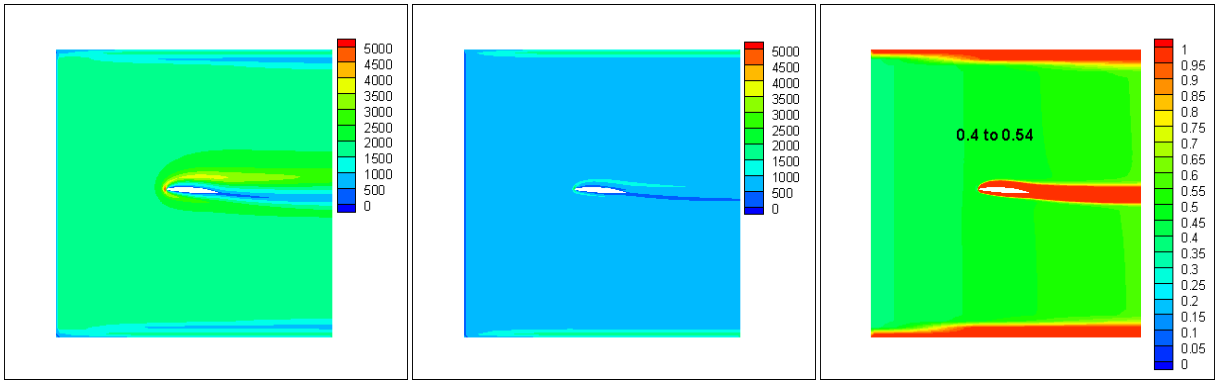

(a) μ_T/μ_L before FBM (b) μ_T/μ_L with FBM (c)$MIN(1,\Delta/(\,k^{1.5}/\varepsilon)$

Figure 10. Comparisons before/after FBM for NACA66MODE hydrofoil, $\mu_T/\mu_L|_{inlet}$=2×10^3,effective *Re*= 1000

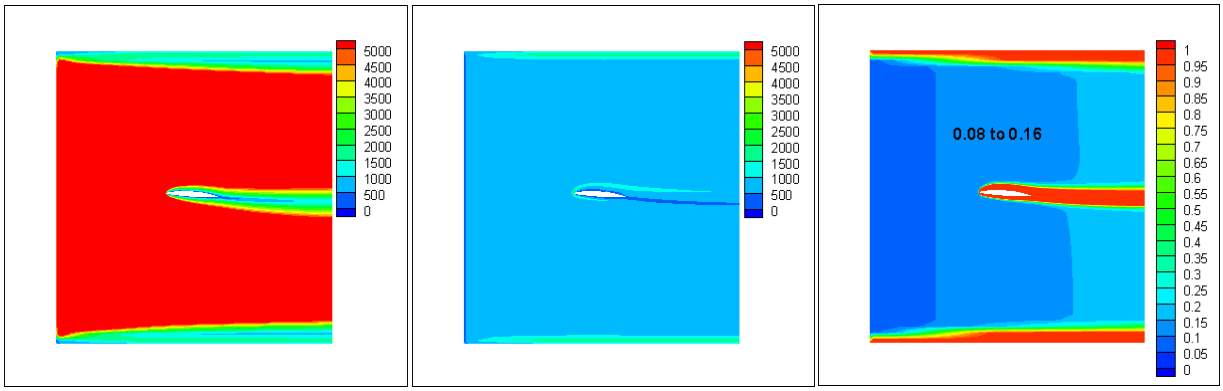

(a) μ_T/μ_L before FBM (b) μ_T/μ_L with FBM (c)$MIN(1,\Delta/(\,k^{1.5}/\varepsilon)$

Figure 11. Comparisons with/without FBM for NACA66MODE hydrofoil, $\mu_T/\mu_L|_{inlet}$=10^4,effective *Re*= 200

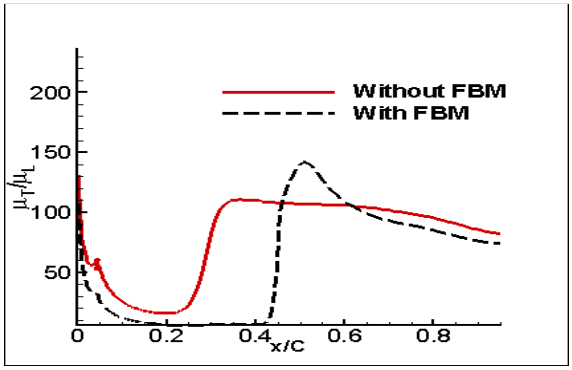

Figure 12. Eddy viscosity near the wall region for NACA66MODE hydrofoil, $\mu_T/\mu_L|_{inlet}$=10^4, effective *Re*= 200

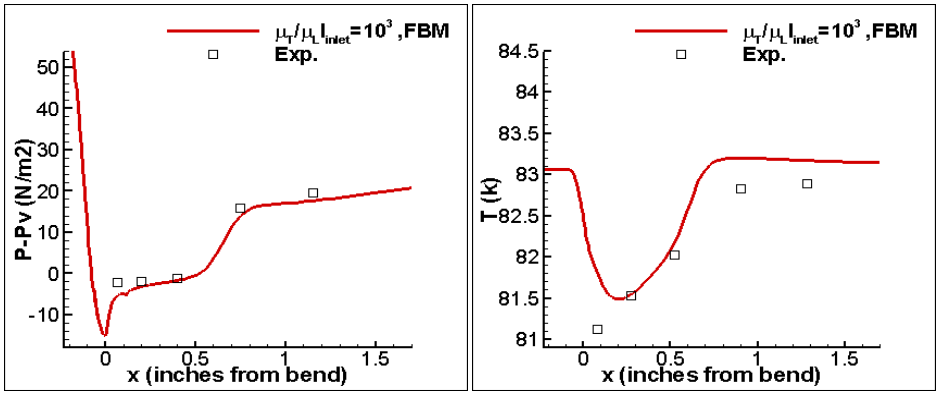

(a) Pressure (b)Temperature

Figure 13. Cryogenic cavitation Case 290C, pressure and temperature along surface by filter-based model with Δ=1.5 maximum grid size ($\mu_T/\mu_L|_{inlet}$=10^3, σ_∞=1.7, *Re*=9.1×10^6, T_∞=83.06K)

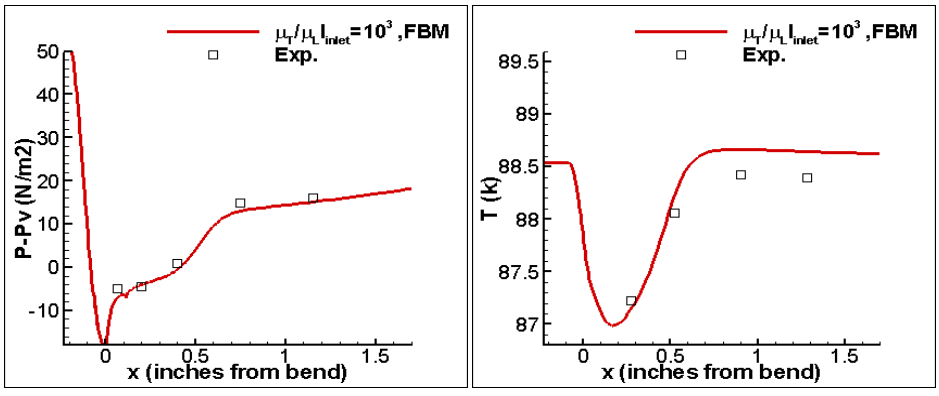

(a) Pressure (b)Temperature

Figure 14. Cryogenic cavitation Case 296B, pressure and temperature along surface by filter-based model with Δ=1.5 maximum grid size ($\mu_T/\mu_L|_{inlet}$=10^3, σ_∞=1.61, *Re*=1.1×10^7, T_∞=88.54K)

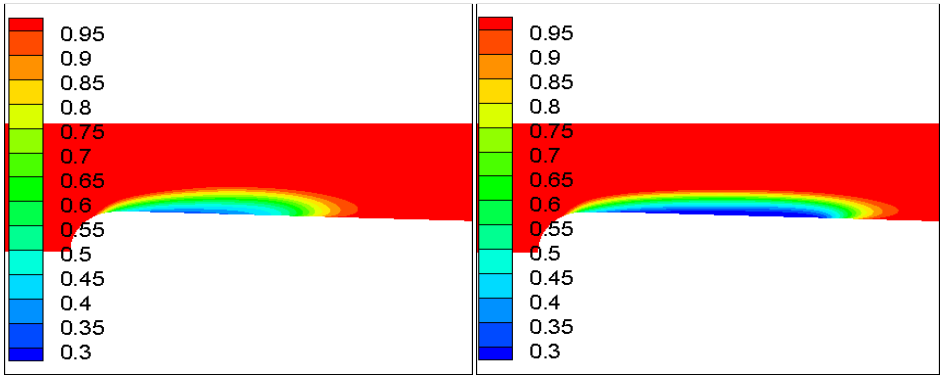

(a) Liq. volume fraction with energy equation (b) Liq. volume fraction without energy equation

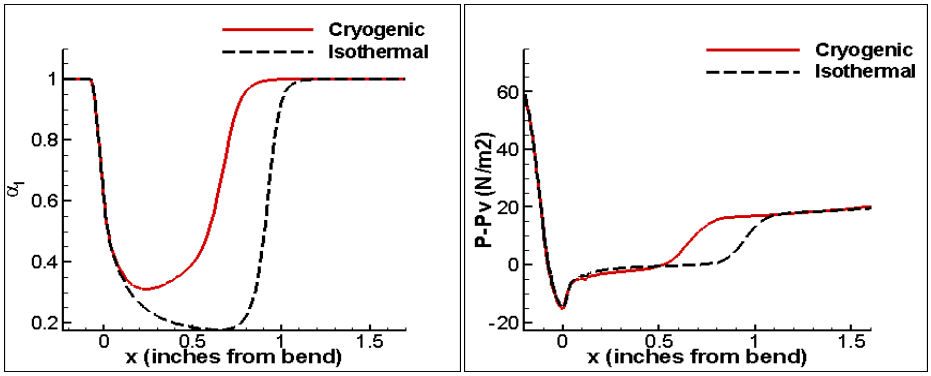

(c) Liq. volume fraction along surface (d)Pressure along surface

Figure 15. Comparisons for cryogenic cavitation Case 290C between results with/without energy equation ($\mu_T/\mu_L|_{inlet}$=10^3, σ_∞=1.7, Re=9.1×10^6, T_∞=83.06K)

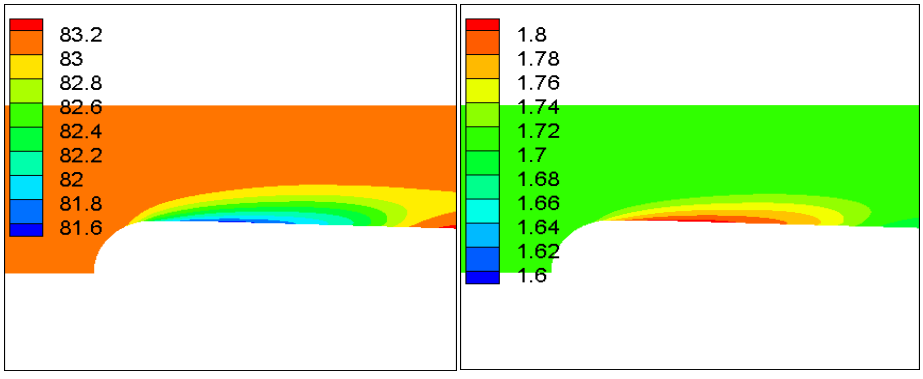

(a)Temperature (b) $\sigma=\sigma(T)$

Figure 16. Cryogenic cavitation Case 290C, the impact of thermal effect on local cavitation number ($\mu_T/\mu_L|_{inlet}$=10^3, σ_∞=1.7, Re=9.1×10^6, T_∞=83.06K)

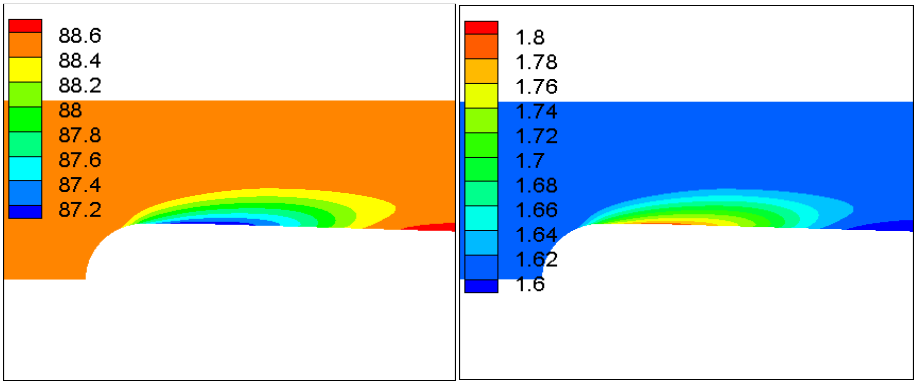

(a)Temperature (b) $\sigma=\sigma(T)$

Figure 17. Cryogenic cavitation Case 296B, the impact of thermal effect on local cavitation number ($\mu_T/\mu_L|_{inlet}$=10^3, σ_∞=1.61, Re=1.1×10^7, T_∞=88.54K)